Review

Thermal Sprayed Protective Coatings for Bipolar Plates of Hydrogen Fuel Cells and Water Electrolysis Cells

Tao Liu [1], Youkun Tao [1,*], Yanli Wang [1], Mingfeng Wu [2], Jin Zhang [1], Yang Yu [3], Xingfu Wang [4] and Jing Shao [2,*]

1   School of Science, Harbin Institute of Technology, Shenzhen 518055, China; liutao2021@hit.edu.cn (T.L.);
    22s058065@stu.hit.edu.cn (Y.W.); jinzhang@hit.edu.cn (J.Z.)
2   College of Chemistry and Environmental Engineering, Shenzhen University, Shenzhen 518060, China;
    2100221027@email.szu.edu.cn
3   Faculty of Materials Science, Shenzhen MSU-BIT University, Shenzhen 518172, China;
    6420230024@smbu.edu.cn
4   Key Laboratory of Materials Physics, Institute of Solid State Physics, Chinese Academy of Sciences,
    Hefei 230031, China; wangxingfu@issp.ac.cn
*   Correspondence: taoyoukun@hit.edu.cn (Y.T.); shaojing@szu.edu.cn (J.S.)

Abstract: As one core component in hydrogen fuel cells and water electrolysis cells, bipolar plates (BPs) perform multiple important functions, such as separating the fuel and oxidant flow, providing mechanical support, conducting electricity and heat, connecting the cell units into a stack, etc. On the path toward commercialization, the manufacturing costs of bipolar plates have to be substantially reduced by adopting low-cost and easy-to-process metallic materials (e.g., stainless steel, aluminum or copper). However, these materials are susceptible to electrochemical corrosion under harsh operating conditions, resulting in long-term performance degradation. By means of advanced thermal spraying technologies, protective coatings can be prepared on bipolar plates so as to inhibit oxidation and corrosion. This paper reviews several typical thermal spraying technologies, including atmospheric plasma spraying (APS), vacuum plasma spraying (VPS) and high-velocity oxygen fuel (HVOF) spraying for preparing coatings of bipolar plates, particularly emphasizing the effect of spraying processes on coating effectiveness. The performance of coatings relies not only on the materials as selected or designed but also on the composition and microstructure practically obtained in the spraying process. The temperature and velocity of in-flight particles have a significant impact on coating quality; therefore, precise control over these factors is demanded.

Keywords: thermal spraying; bipolar plates; coating; corrosion; fuel cells and electrolysis cells

1. Introduction

Hydrogen, as an efficient energy carrier, will play a critical role in economic decarbonization by substituting traditional fossil fuels in transportation, power generation, heavy industry and other sectors [1–4]. Hydrogen fuel cells and water electrolysis cells will form the basis of the large-scale application of hydrogen energy, with the former capability of directly converting the chemical energy of hydrogen into electricity [5,6] and the latter splitting water to generate green hydrogen by consuming renewable electricity [7,8]. Alkaline fuel and electrolysis cells, proton exchange membrane fuel and electrolysis cells, and solid oxide fuel and electrolysis cells are the three representative fuel and electrolysis cell technologies. Alkaline fuel and electrolysis cells are already mature techniques and have entered the commercialization stage [3,7,8]. The latter two are attractive types of next-generation technologies due to their respective characteristics, such as high current density and short respond time of proton-exchange membrane fuel cells (PEMFCs) [9] and electrolysis cells (PEMECs) [10,11], high efficiency of solid oxide fuel cells (SOFCs) [12] and electrolysis cells (SOECs) [13]. PEMFCs and PEMECs may be mentioned together as the PEM cells, while SOFCs and SOECs can be referred to as the SOCs in the following text [14].

Figure 1 shows the operating principles of these electrochemical devices. All these cells consist of anodes, cathodes, electrolytes, sealing materials and bipolar plates (BPs), which are the main components forming a single-cell repeating unit.

(a) SOFCs

H$_2$O and excess H$_2$ outlet

Excess air outlet

H$_2$O

e$^-$

O^{2-}

e$^-$ O$_2$

H$_2$

H$_2$ inlet

Air inlet

Anode   O^{2-} conducting electrolyte   Cathode

Anode: H$_2$+O^{2-} → H$_2$O+2e$^-$

Cathode: 1/2O$_2$+2e$^-$ → O^{2-}

Reaction: H$_2$+1/2O$_2$ → H$_2$O

(b) PEMFCs

Excess H$_2$ outlet

H$_2$O and excess air outlet

H$_2$O

e$^-$

H$_2$

H$^+$

e$^-$

O$_2$

H$_2$ inlet

Air inlet

Anode   H$^+$ conducting electrolyte   Cathode

Anode: H$_2$ → 2H$^+$+2e$^-$

Cathode: 2H$^+$+1/2O$_2$+2e$^-$ → H$_2$O

Reaction: H$_2$+1/2O$_2$ → H$_2$O

(c) SOECs

H$_2$ and excess H$_2$O outlet

O$_2$ outlet

H$_2$

e$^-$

O^{2-}

e$^-$

O$_2$

H$_2$O

H$_2$O inlet

Cathode   O^{2-} conducting electrolyte   Anode

Anode: O^{2-} → 1/2O$_2$+2e$^-$

Cathode: H$_2$O+2e$^-$ → H$_2$+O^{2-}

Reaction: H$_2$+1/2O$_2$ → H$_2$O

(d) PEMECs

H$_2$ outlet

O$_2$ and excess H$_2$O outlet

O$_2$

e$^-$

H$_2$

e$^-$

H$^+$

H$_2$O

H$_2$O inlet

Cathode   H$^+$ conducting electrolyte   Anode

Anode: H$_2$O → 2H$^+$+1/2O$_2$+2e$^-$

Cathode: 2H$^+$+2e$^-$ → H$_2$

Reaction: H$_2$O → H$_2$+1/2O$_2$

Figure 1. Schematics and operating principles of SOFCs (**a**), PEMFCs (**b**), SOECs (**c**) and PEMECs (**d**).

The operating principle of SOFCs (Figure 1a) is described as follows [12,15]: the cathode firstly adsorbs oxygen molecules from the oxidant (oxygen or air) and reduces them to oxygen ions. These oxygen ions pass through the O^{2-} conducting electrolyte, arriving at the anode and reacting with the fuels (hydrogen, hydrocarbons, ammonia, etc.) to generate water and electrons. Finally, electrons are transferred from the anode to the cathode through the external circuit to produce electric power. With respect to PEMFCs, a proton exchange membrane (PEM) is used as the electrolyte, i.e., protons (instead of oxygen ions) serve as the charge carriers in PEMFCs, resulting in the generation of water on the cathode side (Figure 1b) [16]. For the electrolysis cells, electrochemical reactions occurring on each electrode are essentially the reverse processes of those occurring in fuel cells. Effectively, the operation of SOECs (Figure 1c) [1] and PEMECs (Figure 1d) [17] is contrary to that of SOFCs and PEMFCs, respectively. Apart from the anodes, cathodes

and electrolyte membranes, sealing materials and BPs are also major components of these electrochemical devices. Sealing materials play a key role in preventing gas (fuel or air) leakage and ensuring electrical insulation [18]. BPs perform multiple significant functions, such as separating the fuel and oxidant, electrically and thermally connecting the cells in series to form a stack, providing mechanical support, etc. [19].

Currently, the large-scale application of hydrogen fuel cells and electrolysis cells is mainly impeded by the high manufacturing cost of these devices [20], in which the BP components account for a major portion. The initial BPs are conventionally made of expensive and difficult-to-process materials (e.g., $LaCrO_3$-based ceramics for SOC cells [21] and titanium plates for PEM cells [2,22]), accounting for ~30% and ~53% of the cost for SOC and PEM cells, respectively [2,23]. It is, therefore, of great interest to lower the cost by employing low-cost and easy-to-process alternative metal materials (e.g., ferritic stainless steels for SOC cells and stainless steels, aluminum or copper for PEM cells) [24,25]. Unfortunately, owing to the poor chemical stability, these candidate materials are susceptible to corrosion, resulting in a series of problems (such as Cr poisoning in SOCs, decrease in proton conductivity in PEM cells, etc.) during the electrochemical operation [26–28]. Therefore, improving the corrosion resistance of these BP materials is an essential prerequisite for the use of hydrogen fuel cells and electrolysis cells.

Protective coatings, which are aimed to isolate the substrate material from external corrosive environments, have been employed for the protection of BPs from corrosion [29,30]. An effective coating should possess the following features: (i) it must be inert or chemically stable, ensuring that no continuous reaction occurs between the coating material and the external corrosive environment; (ii) it must be dense and integral to block corrosive medium permeation; (iii) it must be electrically conductive so as to enhance electron conducting; (iv) it must have a similar thermal expansion coefficient with the metallic substrate, in order to minimize formation of any micro- and macro-cracks due to thermal stress along with temperature change. Based on the above requirements, coating materials that have been explored for protecting metallic BPs of PEMFC or PEMEC from electrochemical corrosion mainly include: (i) noble metals (Pt [31], Au [32]); (ii) transition metals (Nb [33], Ti [34]); (iii) transition metal nitrides (CrN [35], TiN [36]). Similarly, rare-earth perovskite oxides [37,38] and spinel oxides [29] are the most commonly used materials to protect ferritic stainless-steels (FSS) BPs from corrosion in SOCs [14]. Apart from coating materials, coating technology (such as physical vapor deposition [31], electroplating [32] and metal nitriding methods [36] for PEMFC and PEMEC; slurry coating [24], magnetron sputtering (MS) [29] and electrophoretic deposition (EPD) [29] for SOCs) is another critical factor determining the coating performance because it directly affects the coating microstructure and composition. Currently, some coating materials have shown potential application prospects; for example, Nb-coated stainless steel BPs exhibited a low degradation rate (~5.5 $\mu V\ h^{-1}$) during the 14,000 h electrolysis cell test [39]. Mn-Co spinel-coated FSS BPs showed excellent stability over the 40,000 h SOFC stack test [40]. Therefore, the current research focuses on developing suitable coating technologies for commercial applications; the advantages and disadvantages of different coating methods for BPs are summarized in Table 1. Slurry coatings, electrophoretic deposition, physical vapor deposition and electrodeposition are commonly used coating methods for SOCs; the first two use spinel ceramic powders as feedstocks to deposit coatings, the as-prepared coatings are porous and need to improve coating density through reduction and re-oxidation heat treatment. The latter two are used to prepared metal or alloy coatings and also need oxidation heat treatment to convert these coatings into spinel coating. Hence, all of these coating methods are time-consuming and low efficiency. Metal nitriding, physical vapor deposition, chemical vapor deposition and electroplating are commonly used coating methods for PEMFCs and PEMECs, unfortunately, all of these coating technologies are unsatisfactory due to their respective disadvantages.

**Table 1.** Advantages and disadvantages of different coating methods for BPs.

Coating Method for BPs of SOCs			
Coating method	Advantages	Disadvantages	Structure feathers
Slurry coatings	Simple, low cost	Low efficiency, post-treatment needed	Porous and nonuniform
Electrophoretic deposition	Low cost, non-line-of-sight process	Post-treatment needed	Porous
Physical vapor deposition	Dense coating	Time-consuming for a thick coating, high vacuum condition, unsuitable for mass production, post-treatment needed	Dense and uniform
Electrodeposition	Lost cost, uniform coating thickness	Difficulty for binary or ternary alloy deposition, post-treatment needed	Dense and uniform
Atmospheric plasma spraying	Simple, cost-effective, suitable for mass production	Dependent on line-of-sight, some porosities and micro-cracks in the coating	Dense
Coating method for BPs of PEMFCs and PEMECs			
Metal nitriding	Coating with low incidence of pinhole defects	High-temperature operation	Dense and uniform
Physical vapor deposition	Coating with good adherence	BP size limited by vacuum chamber, pitting corrosion, high vacuum condition	Dense and uniform
Chemical vapor deposition	Suitable for mass production, coating with good corrosion resistance	High-temperature operation, high vacuum condition	Dense and uniform
Electroplating	Coating with uniform thickness	Suitable for conductive materials, poor adherence	Dense and uniform
Vacuum plasma spraying	high deposition rate, thick film	micro-cracks and open pores, dependent on line-of-sight, high vacuum condition	Dense
High-velocity oxygen fuel spraying	High deposition rate, thick film	Dependent on line-of-sight, suitable for alloy or non-oxide ceramic materials with low melting point	Dense

Among various coating technologies, thermal spraying [41,42] is the most promising and cost-effective method due to its high deposition rate, suitability for mass production and relatively low cost, which has attracted great interest, especially from the industry. Thermal spraying is a direct melt–spray–deposition process in which the raw powders are fed into a high-temperature flame, heated to a molten or semi-molten state and propelled toward a pre-treated substrate with high velocity. Then, the coating is built up through continuous impingement and rapid solidification of the droplets. The deposition principle of thermal spraying is shown in Figure 2a [43]. According to the differences in energy sources, thermal spraying can be divided into a few categories, as shown in Figure 2b [44]. Among these technologies, atmospheric plasma spraying (APS), vacuum plasma spraying (VPS) and high-velocity oxygen fuel (HVOF) spraying are commonly used technologies for coating BPs. These technologies are very suitable for rapidly preparing coatings with micron-sized dimensions rather than nano-scaled thin films. Both APS and VPS use a high-velocity plasma jet to melt coating materials. The differences between them are that the former deposits coating in an air atmosphere, and the latter operates in an inert and low-pressure/vacuum atmosphere. Unlike APS and VPS, HVOF uses a high-temperature flame originating from the combustion of fuel (e.g., propane, acetylene, kerosene or propylene) to melt down the coating materials. The characteristics of these technologies are shown in Figure 2c [45]. Due to significant differences in the atmosphere, flame temperature and flame speed among these three spraying technologies, the appropriate coating materials for spraying vary significantly as well. Figure 2d–f illustrates the spraying mechanisms (inset maps) and the photographs of APS, VPS and HVOF, respectively. In addition, various bipolar plates used in SOCs and PEM cells are shown in Figure 2g–j.

The key to obtaining high-quality thermal sprayed coatings (such as uniform thickness, good electrical conductivity, excellent corrosion resistance, etc.) lies in precise control of the coating composition and micro-structure, which mainly depends on the spraying parameters. One of the consequences caused by improper spraying parameters is powder overheating, which results in powder decomposition and composition deviation from its initial stoichiometric ratio. Therefore, the high-temperature oxidation resistance and conductivity of the as-sprayed coating may be unsatisfactory [46]. Moreover, a mismatch in the coefficients of thermal expansion (CTE) between coatings and substrates will induce thermal stresses, leading to the formation of defects (such as micro-cracks or pores) in coatings [47–49]. The defects could provide channels for the corrosive medium to penetrate

the substrate material, leading to deterioration of the oxidation/corrosion resistance of the as-sprayed coatings. Therefore, a better understanding of the relationship between the spraying process, coating characteristics and coating performance is critical for further improving the coating quality. This review focuses on the characteristics and applicability of three different thermal spraying technologies, including APS, VPS and HVOF, which have been intensively studied for coating BPs in several major categories of hydrogen fuel cells and electrolysis cells. The technological features, strengths and limitations of these methods are summarized and analyzed. The effect of spraying parameters on detailed coating composition and microstructure, as well as the corrosion resistance and electrical conductance, are reviewed for the individual thermal spraying technologies.
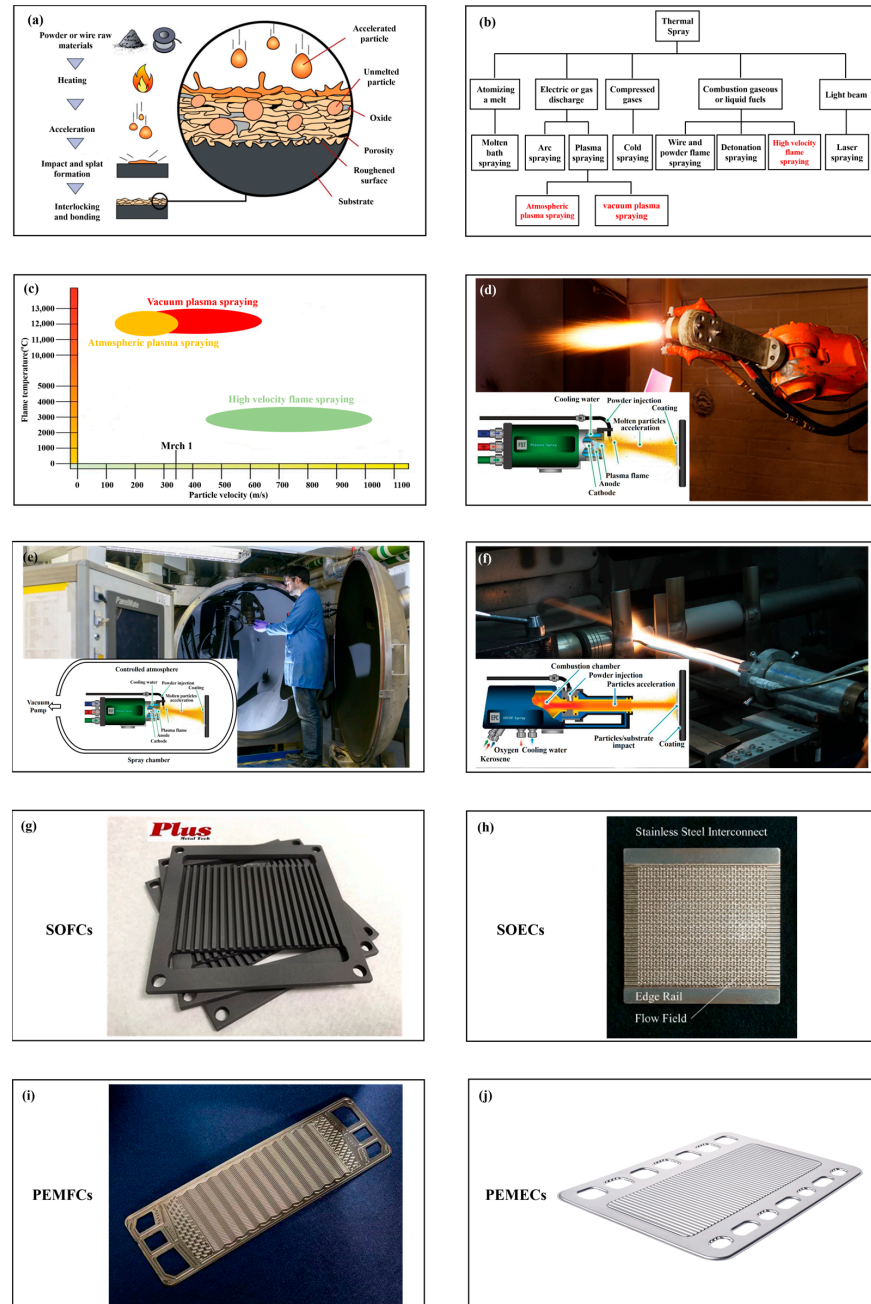
Figure 2. Deposition principle (**a**) of thermal spraying [43]; classification of the thermal spraying technologies (**b**) [44]; particle temperature and velocity characteristics of APS, VPS and HVOF (**c**) [45]; actual photographs and spraying mechanisms (inset maps) of APS (**d**), VPS (**e**) and HVOF (**f**); various bipolar plates used in SOFCs (**g**), SOECs (**h**), PEMFCs (**i**) and PEMECs (**j**).

2. Atmospheric Plasma Spraying

2.1. Features and Strengths of Atmospheric Plasma Spraying

During the APS process, plasma is used to heat the feedstock in air atmospheres. Therefore, materials that are sensitive to oxygen or unstable at high temperatures (such as metals, alloys or non-oxide ceramics) are not used in APS coating processes. APS is mainly applied to prepare oxide coatings. In SOCs, typically rare-earth perovskite oxides and spinel oxides are used, which decrease the growth rate of thermally grown oxide (TGO) and limit the outward migration of Cr species [50].

APS is more suitable for the rapid preparation of dense coatings without post-heat treatment compared to traditional wet chemical methods (such as brush painting [50], screen printing [51,52] and wet powder spraying [53]). Therefore, APS is more attractive than traditional wet chemical methods in depositing rare-earth perovskite oxide and spinel oxide coatings for BP protection. In traditional wet chemical methods, slurries composed of raw powder, solvent, dispersant and binder are deposited onto substrates to form a green coating, which is subsequently dried and sintered to form the desired coating structure [54]. However, these coating preparations are time-consuming due to the additional drying and sintering processes [55–57] compared to APS. Furthermore, several parallel production lines are usually needed to reach a high production capability, leading to increased equipment costs [58]. In contrast, APS offers a cost-effective option for producing BP coatings. Varied materials, e.g., rare-earth perovskite oxides, spinel oxides, etc., can be directly deposited on BP substrates using one single APS equipment (no need for extra sintering treatment). Meanwhile, APS has the ability to achieve BP coatings within a few minutes due to the high deposition rate (a few kilograms of feedstock per hour) [58]. In addition, the microstructure and composition of coatings can be precisely controlled by adjusting spraying parameters except for some special specimens (such as extremely dense or porous coatings).

2.2. Application of APS-Sprayed Coatings in SOFCs

Ferritic stainless steels containing 17–25 wt.% Cr (e.g., Crofer 22 APU, SUS 430 and 441, SMG 232) are often used as BP substrate materials for SOFCs and SOECs due to appropriate CTE, excellent mechanical properties and high electrical conductivity [50,59,60]. FSS BPs are exposed to both reducing atmospheres (SOFC anode and SOEC cathode) and oxidizing atmospheres (SOFC cathode and SOEC anode) [61,62] during the cell operation. Oxidation corrosion of FSSs mainly occurs in the oxidizing atmosphere to form metal oxides (such as Fe_2O_3, Cr_2O_3 and $MnCr_2O_4$) [63–66], resulting in performance degradation and life-shortening of SOFCs and SOECs. The cross-sectional morphology of the oxide scales grown on the air side of FSS BPs, which was exposed to fuel–air dual atmospheres, is shown in Figure 3a. The degradation mechanisms of FSSs are listed as follows: (i) Ohmic resistance increase [29], where the growth of oxide scale with low conductivity is one of the important reasons for the increase in ohmic resistance in BPs. Oxidation of FSSs leads to the formation of a low-conductivity oxide layer composed of Cr_2O_3 (0.006–0.16 S·cm^{-1}) (inner layer) and $MnCr_2O_4$ (0.02–0.4 S·cm^{-1}) (outer layer) [29]. With the time increasing, the oxide scale (mainly Cr_2O_3) thickens and thereby increases the ohmic resistance of BPs. Moreover, the iron oxides, which tend to destroy the originally dense layer of Cr_2O_3 and $MnCr_2O_4$ and promote inward diffusion of oxygen, will further accelerate the growth of the Cr_2O_3 layer and thereby increase the ohmic resistance of BPs [63,67]. S. Fontana et al. [68] investigated the electrical behavior of bare Crofer 22 APU and found its area-specific resistance (ASR) value exceeded the maximum target (100 mΩ·cm^2) [69] for BP materials after 7700 h in air at 800 °C. (ii) Air electrode poisoning [26], where chromium oxide (Cr_2O_3), which is thermodynamically unstable at the cathode of SOFCs or anode of SOECs, can react with oxygen and/or water to generate gaseous high valence Cr species (CrO_3 or $CrO_2(OH)_2$) [26]. Subsequently, these gaseous Cr species are transported towards the cathode of SOFCs or anode of SOECs. They are finally reduced to form solid Cr_2O_3 or Mn-Cr spinel at the air electrode–electrolyte–gas triple-phase boundary when $La_{1-x}Sr_xMnO_3$ is used as the air electrode. Because the air electrode–electrolyte–gas triple-phase boundary is the critical

active site where the O_2 reduction reaction occurs, Cr_2O_3 or Mn-Cr spinel deposited at this place will severely inhibit the O_2 reduction reactions [26]. A scheme of the reaction steps of oxygen reduction on the $La_{0.72}Sr_{0.18}MnO_3$ electrode in the presence of FSSs BPs is shown in Figure 3b [67]. Similarly, migration of Cr species also poisons (La-Sr)CoO$_3$ and (La-Sr)(Co,Fe)O$_3$ electrode materials by forming $SrCrO_4$ [26].

Through the above introduction, it can be concluded that the degradation of FSS BPs could be mitigated by limiting the growth rate of Cr_2O_3 and enhancing the thermodynamic stability of Cr_2O_3. Rare earth perovskite oxides [46] and spinel oxides [50,70], which have excellent high-temperature oxidation resistance and electrical conductivity, can be adopted to cope with these challenges. Therefore, these materials are frequently used for coating the FSS BPs of SOFCs and SOECs.
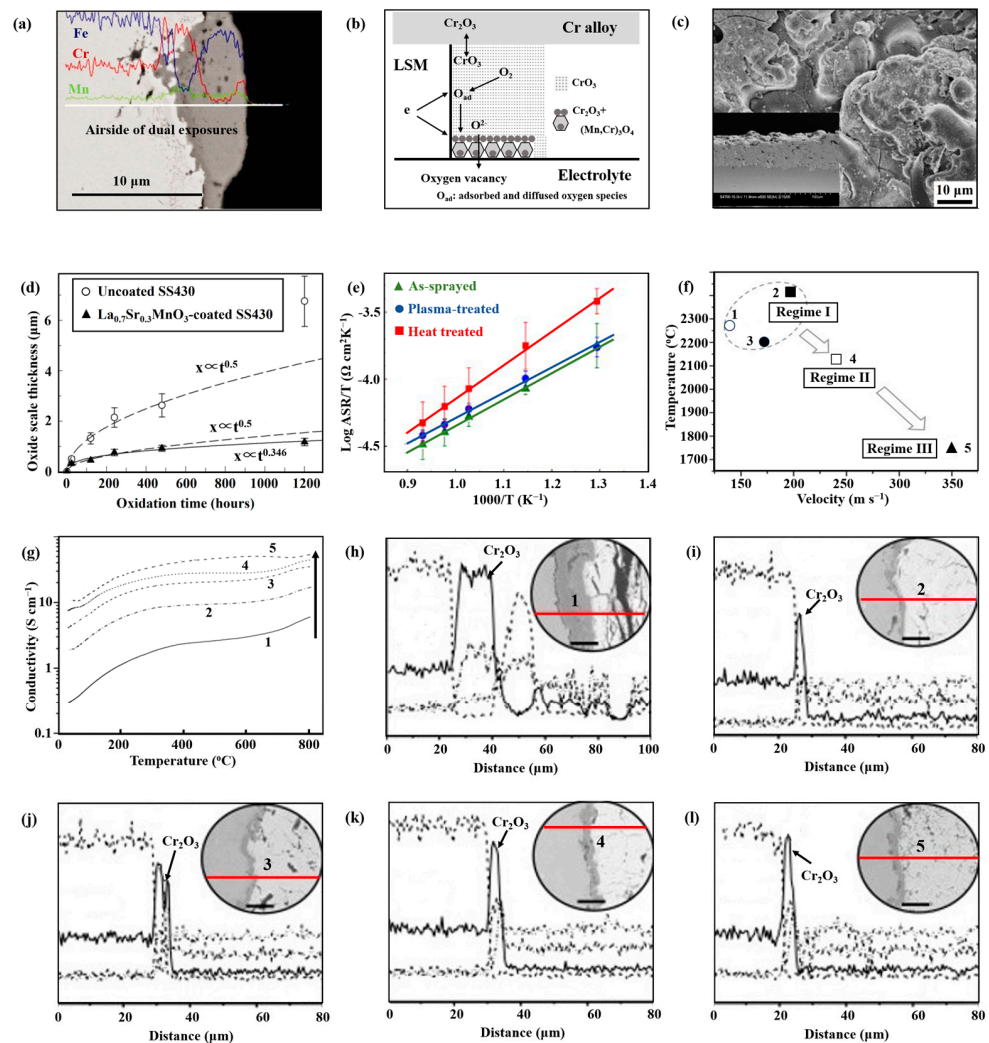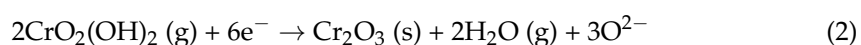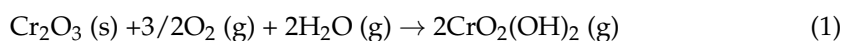

Figure 3. Cross-sectional morphology (**a**) [64] of the oxide scale on the air side for an FSS BP sample tested in fuel/air dual atmospheres; schemes of the reaction steps (**b**) [67] for oxygen reduction on the $La_{0.72}Sr_{0.18}MnO_3$ electrode in the presence of FSSs BPs; surface and cross-sectional images (inset) (**c**) [71] of APS-sprayed $La_{0.8}Sr_{0.2}MnO_3$ coating; thickness of TGO scale (**d**) [72] for uncoated and $La_{0.7}Sr_{0.3}MnO_3$-coated samples as a function of oxidation time at 800 °C; temperature dependence of ASR for as-sprayed and post-treated samples (**e**) [71]; temperature–velocity map of the $(La_{0.8}Sr_{0.2})_{0.99}MnO_3$ in-flight particles in APS process (**f**) [46]; temperature-dependent in-plane electrical conductivities of the samples (**g**) [46]; corresponding SEM/EDX analysis (**h**–**l**) [46] after 600 h oxidation at 800 °C. Reprinted from [64,67,72] with permission from IOP Publishing, from [46,71] with permission from Elsevier.

2.2.1. Application of APS-Sprayed Rare Earth Perovskite Oxide Coatings

Rare-earth perovskite oxides, e.g., the $La_{1-x}Sr_xMnO_3$ (Figure 3c), are attractive coating materials due to their high electrical conductivity, suitable CTE and oxidation resistance at high temperatures [71–74]. Baik et al. [72] produced $La_{0.7}Sr_{0.3}MnO_3$ feedstock powder with near-spherical morphology and a mean powder size of 25 μm through solid-state reaction and spray drying, deposited $La_{0.7}Sr_{0.3}MnO_3$ on 430 by APS, and investigated the effectiveness of this as-sprayed $La_{0.7}Sr_{0.3}MnO_3$ coatings (Figure 3d) for improving high-temperature oxidation resistance and ASR of FSS BPs [72]. After a 1200 h oxidation test at 800 °C in air, the Cr_2O_3 growth was only 1.5 μm in thickness for the coated FSS sample. Accordingly, a low ASR of 10 mΩ·cm² was obtained, almost one order of magnitude lower than the uncoated sample. Moreover, a SOFC stack test using $APS-Ni_{80}Cr_{20}/(La_{0.75}Sr_{0.25})_{0.95}MnO_3$ coated BPs also proves the coating effectiveness in protecting FSS substrates from oxidation, as no performance decay was detected. In contrast, the stack equipped with uncoated BPs showed a degradation rate of 4.4% per hundred hours [73].

The performance of $La_{1-x}Sr_xMnO_3$ coating can be significantly influenced by spraying parameters, such as gas ratios, torch current and spraying distance, as shown in Table 2. Owing to high plasma flame temperature (above 10,000 K), phase decomposition of $La_{1-x}Sr_xMnO_3$ caused by overheating of powder particles is almost inevitable during the spraying process. This results in the selective evaporation of Mn, which reduces the electrical conductivity of the as-sprayed coating (Figure 3e) [71]. Fortunately, the loss of Mn could be effectively limited by adjusting the spraying parameters. Han et al. [46] used commercial $(La_{0.8}Sr_{0.2})_{0.99}MnO_3$ (LSM) powder (particle size range: 20–53 μm) to deposit coating and investigated the spraying processes. They found that plasma flame temperature and velocity had significant impacts on coating composition and microstructures, which ultimately determined the oxidation resistance and electrical properties. Figure 3f presents a temperature–velocity map of the $(La_{0.8}Sr_{0.2})_{0.99}MnO_3$ in-flight particles. A higher flame temperature and lower flame velocity indicated that the $(La_{0.8}Sr_{0.2})_{0.99}MnO_3$ particles would absorb more heat, favoring a denser coating structure. On the other hand, it may result in the decomposition of LSM and loss of the Mn and O contents in the as-sprayed coating. The loss of Mn promoted the formation of low-conductivity La_2O_3. With an increase in the La_2O_3 amount, the electrical conductivity of coatings reduced from 55 to 6 S cm^{-1} (Figure 3g). Moreover, the hygroscopic La_2O_3 promoted the water absorption and its diffusion within the coating, increasing the growth rate of the Cr_2O_3 layer through Equations (1) and (2) [46], which are listed as follows:

$$Cr_2O_3 \text{ (s)} + 3/2O_2 \text{ (g)} + 2H_2O \text{ (g)} \rightarrow 2CrO_2(OH)_2 \text{ (g)} \tag{1}$$

$$2CrO_2(OH)_2 \text{ (g)} + 6e^- \rightarrow Cr_2O_3 \text{ (s)} + 2H_2O \text{ (g)} + 3O^{2-} \tag{2}$$

Therefore, after 600 h oxidation at 800 °C, the TGO layer reached 30 μm in thickness for the samples with 44 wt.% Mn loss, while the samples with only 0.7 wt.% Mn loss showed limited growth of TGO below 3 μm. Cross-sectional SEM images and the corresponding EDS line profiles of different samples are shown in Figure 3h–l. The loss of O also caused a decrease in the electrical conductivity of the as-sprayed coating. However, O-loss could be recovered through thermal exposure in the oxidizing atmospheres after the startup of SOCs. Therefore, reducing the loss of Mn through spraying parameter optimization is of critical importance to limit the destructive effect of La_2O_3 and obtain a high-quality $La_{1-x}Sr_xMnO_3$ coating.

Table 2. Deposition parameters of different thermal sprayed coatings.

Atmospheric Plasma Spraying										
Powder	Torch	Ar /L·min^{-1}	H$_2$ /L·min^{-1}	I /A	Power /kW	Particle Velocity/m·s^{-1}	Particle Temperature /°C	Conductivity /S·cm^{-1}	Thickness of Thermally Grown Oxide/µm	Ref.
LSM	F4 8 mm	35	10	650	42.9	139	2276	6	30	[46]
		60	6	700	47.3	198	2425	17	2	
		60	3	400	23.5	171	2192	38	2	
	F4 6 mm	60	3	550	29.7	242	2137	43	2	
	SG100	90	35 (He)	590	39.2	350	1725	55	2	
MCO	F4 8 m	35	10	650	42.9	127	2281	11	52	[75]
		60	3	400	23.5	154	2087	19	36	
		60	6	700	47.3	212	2318	7	1	
	F4 6 mm	60	3	550	29.7	345	2251	22	6	
	SG100	90	35 (He)	590	39.4	580	2360	38	1	
Vacuum plasma spraying										
Powder	Plasma enthalpy (MJ·kg^{-1})				Leak rate (mbar·cm^{-2} s^{-1})					Ref.
Ti	14.62				12.6					[34]
	14.66				10.5					
	21.27				4.3					

## 2.2.2. Application of APS-Sprayed Spinel Oxide Coatings

Electrically conductive spinel oxides, such as Mn-Co [74,76] and Cu-Mn [77,78] spinels, exhibit superior performance in obstructing outward migration of Cr and inward migration of O (compared to rare-earth perovskite oxides) [79], are typically used to protect FSS BPs from high-temperature oxidation in solid oxide cells. An example of Mn$_{1.5}$Co$_{1.5}$O$_4$ coating prepared via APS technology is illustrated in Figure 4a [80]. However, during the spraying process, selective evaporation of Mn with spinel decomposition may occur, resulting in a deviated coating composition from that of the feedstock [71]. Furthermore, thermal reduction occurring under high temperatures could promote the structure transformation of Mn-Co spinel into the (Mn,Co)O rock salt phase, an insulator (8.2×10^8 ohm) significantly impairing the electrical conductivity of the coating [81]. Fortunately, both the selective evaporation of Mn and the content of (Mn,Co)O rock salt phase can be controlled by optimizing the spraying parameters. In addition, the (Mn,Co)O rock salt phase could be transformed into a spinel phase through heat exposure in air atmosphere.

Han et al. [75] used commercial Mn$_{1.5}$Co$_{1.5}$O$_4$ (MCO) powder as feedstock (particle size range: 15–45 µm) to deposit coating and investigated the effect of the APS characteristic operating parameters on MCO coatings; a detailed summary of spraying parameters is shown in Table 2. The plasma flame characteristics (temperature and velocity) were adjusted by controlling plasma H$_2$ content, overall gas mass flow rate, applied power and spray hardware configurations. The temperature and velocity map of flying particles is shown in Figure 4b. They found that increasing the absorbed heat of MCO particles resulted in a higher content of rock salt phase ((Co,Mn)O), providing longer electron hopping distance and thereby decreasing the conductivity of the coating from 40 to 6 S cm^{-1} (Figure 4c,d). At the same time, a higher thermal stress was generated due to a faster cooling rate, which in turn led to micro-cracks in the coating. These micro-cracks provided channels for the inward diffusion of oxygen in the coating, whereby the high-temperature oxidation resistance deteriorated. The growth of chromium oxide scale ranging from 1 to 50 µm in thickness is shown in Figure 4e–i for BP samples with different coatings [75]. Properly absorbing the heat of particles by using appropriate power and flame velocity is critical to restrain the formation of rock salt phase and micro-cracks, thereby being beneficial to achieve a high-quality spinel coating.

R. Vaβen et al. [82] deposited Mn-Co-Fe spinel powder (chemical composition: 23.5 wt.% Mn, 47.6 wt.% Co, 2.4 wt.% Fe and 26.5 wt.% O) on Crofer 22 APU substrate and systematically studied the effect of phase transformation on the coating microstructure, high-temperature oxidation resistance and Cr diffusion resistance. Oxygen content (22.2 ± 0.3 wt.%) in the as-sprayed coating was significantly lower than that in the feedstock powder (26.4 ± 0.7 wt.%) and almost completely recovered (26.7 ± 0.1 wt.%) after

heat-treatment, indicating that the appearance of (Mn,Co,Fe)O rock salt phase was due to oxygen loss during the spraying process and the recovery of Mn-Co-Fe spinel phase was caused by the chemical reaction between (Mn,Co,Fe)O rock salt phase and oxygen during the heat treatment [83]. The oxygen uptake in the heat treatment process resulted in a volume expansion of the coating, which improved the coating integrity and continuity by crack healing. A schematic diagram of the crack-healing process in air is shown in Figure 4j–l [82]. Therefore, the high-temperature oxidation resistance and Cr diffusion resistance of the coating after crack healing had been greatly improved compared to the as-sprayed coating. According to the data of a SOFC stack equipped with Mn-Co-Fe spinel-coated BPs after 33,000 h operation, the degradation rate of this stack was only 0.2% per 1000 h [84], which basically meets the technical requirements of the U. S. Department of Energy [85].
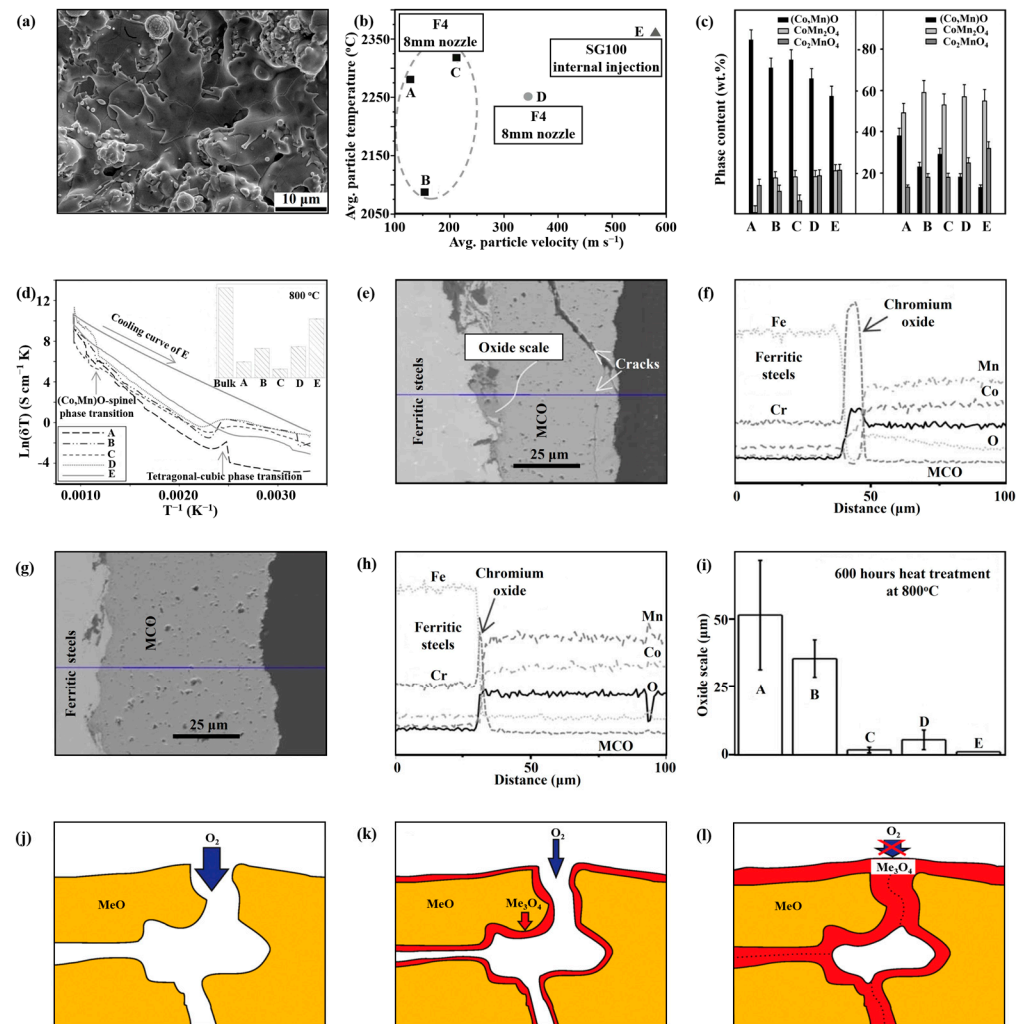

Figure 4. Surface morphologies (**a**) [80] of the APS-sprayed $Mn_{1.5}Co_{1.5}O_4$ coatings; temperature–velocity map (**b**) [75] for the in-flight particles in APS process; phase content (**c**) [75] in the coating as-sprayed or annealed at 700 °C for 2 h; temperature-dependent electrical conductivity of A–E coatings (**d**) [75] up to 800 °C; Inset: bulk material and as-sprayed coatings (**d**); cross-sectional SEM (**e**) [75] and EDX (**f**) [75] results of sample B; SEM (**g**) [75] and EDX (**h**) [75] results of sample E after 600 h oxidation at 800 °C; growth of oxide scales of the as-sprayed coatings under different spray parameters of (**b**) at 800 °C in 20 h (**h**) and 600 h (**i**) [75]; schematic diagram of the crack-healing process in air: as-sprayed coating (**j**); phase transformation from MeO rock salt structure to spinel structure (**k**); coating after the cracks are closed (**l**) [82]. Reprinted from [75,80,82] with permission from Elsevier.

2.3. Application of APS-Sprayed Coatings in SOECs

As mentioned in Section 2.2, high-temperature oxidation of the FSS BPs mainly occurs on the SOFC-cathode and SOEC-anode sides [86]. Although both cases are exposed to oxygen-containing gases, the latter is actually experiencing a more harsh oxidizing condition, which can be explained in two aspects: (i) A high temperature is conducive to improving the hydrogen production efficiency; therefore, the SOECs' operating temperature is usually higher than that of SOFCs, bringing more stringent technical demands on the coating stability throughout its lifespan [45]. (ii) The water vapor content in the intake of SOECs is much higher than that of SOFCs. Also, the oxygen partial pressure of the SOEC anode (e.g., pure oxygen) is normally much higher than that of the SOFC cathode (air). Therefore, a better high-temperature oxidation resistance is demanded for BPs operating in SOECs compared to SOFCs [87].

$La_{1-x}Sr_xMnO_3$ coating prepared by APS on FSS BPs has been proven to be effective in oxidation resistance during SOFCs' operation. Also, the same coating has been attempted to protect FSS BPs from oxidation in SOECs. Lorenzo et al. [88] deposited $La_{1-x}Sr_xMnO_3$ coating on the surface of Crofer 22 APU through APS and slurry, respectively, and evaluated the performance of these samples in pure water vapor and pure oxygen at 850 °C and 30 bar. The high-temperature oxidation resistance of the APS-sprayed $La_{1-x}Sr_xMnO_3$ coating was inferior to that of the slurry-coated one due to the breakaway oxidation (i.e., the rapid growth of Fe-rich oxides on alloys initially forming protective Cr-rich oxide scales). The author speculated that the failure of APS-sprayed $La_{1-x}Sr_xMnO_3$ coating might be due to the Cr depletion of the substrate, although they did not provide direct evidence [88]. Hence, further verification is needed for the APS-sprayed $La_{1-x}Sr_xMnO_3$ coatings to be used in SOECs. Figure 5a illustrates the cross-sectional morphology of an APS-$La_{1-x}Sr_xMnO_3$ coated sample and its corresponding EDX mapping after exposure at 850 °C and 30 bar in dry pure oxygen for 3000 h [88].
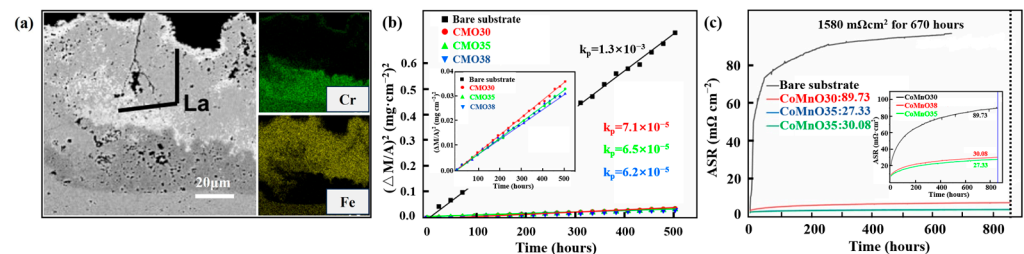
Figure 5. Cross-sectional SEM/EDS of $La_{1-x}Sr_xMnO_3$-coated sample (**a**) [88] after exposure at 850 °C and 30 bar in dry pure oxygen for 3000 h, oxidation kinetics (**b**) [89] and ASR values (**c**) [89] of the uncoated and coated samples as function of time. Reprinted from [88,89] with permission from Springer Nature.

The applicability of APS-spinel coatings for BPs working under SOEC anode conditions is also explored. According to the study of Cheng et al., [89] APS-sprayed Mn-Co spinel coatings significantly improved the high-temperature oxidation resistance and conductivity of the substrates (AISI 441). It has been found that the oxidation kinetics coefficient of the coated samples ($MnCo_2O_4$-30 kW, $MnCo_2O_4$-35 kW and $MnCo_2O_4$-38 kW) was two orders of magnitude lower than that of the uncoated sample, resulting in an oxide layer much thinner for the coated samples (1.5–2 μm) than the uncoated sample (80–168 μm). Oxidation kinetics for uncoated and coated samples are shown in Figure 5b [89]. Meanwhile, the ASR of coated samples ($MnCo_2O_4$-30 kW: 89.73 mΩ cm^2, $MnCo_2O_4$-35 kW: 27.33 mΩ cm^2, $MnCo_2O_4$-38 kW: 30.08 mΩ cm^2) was lower than that of the uncoated sample (1.58 Ω cm^2). ASR values of uncoated and coated samples are shown in Figure 5c [89].

3. Vacuum Plasma Spraying

3.1. Features and Strengths of Vacuum Plasma Spraying

Vacuum plasma spraying (VPS) is a unique and advanced thermal spraying technology distinguished from the common atmospheric plasma spraying (APS). The key characteristic of VPS is that the spraying is conducted in low-pressure inert atmospheres (e.g., Ar), which prevents metal feedstock from being oxidized, ensuring a high electrical conductivity of the as-sprayed coating. Therefore, VPS can be used to prepare metallic coatings for BPs of PEM fuel cells or electrolysis cells.

Compared to the traditional technologies for depositing thin metal films (a few microns or below in thickness), such as chemical vapor deposition or physical vapor deposition (e.g., magnetron sputtering), VPS holds a big advantage of the capability to rapidly prepare thick protective coatings. Thin protective films, e.g., Nb films in a few microns thickness, can hardly protect the stainless-steel substrate from corrosion, particularly for the anode side of PEM electrolysis cells where a harsh electrochemical corrosion environment (i.e., high potential, oxygen saturation and acid medium) exists. A thick coating of dozens of microns or more is beneficial to the elimination of defects like the pinhole that often impairs the substrate with pitting corrosion [90]. Hence, coatings prepared by thermal spraying have better corrosion resistance than those deposited through chemical vapor deposition or physical vapor deposition. Meanwhile, the conductivity of VPS-sprayed metallic coatings is better than that of APS-sprayed metallic coatings by preventing metallic powder oxidation. Therefore, VPS is more suitable than APS for BP protection of PEM electrolysis cells, while VPS equipment is more expensive than APS [91]. With a high deposition rate of a few kilograms of feedstock per hour, VPS is advantageous in preparing thick metallic coatings so that the corrosion resistance of BPs can be greatly enhanced, especially for the PEM electrolysis cells.

3.2. Application of VPS-Sprayed Coatings in PEM Cells

Low-cost and easy-to-process metallic materials, such as stainless steel, copper or aluminum, are prone to corrosion in PEM cells. Particularly when serving on the anode side in PEM electrolysis cells, the commonly used metallic substrates of BPs are vulnerable to electrochemical oxidation and corrosion in the harsh operating environment (high potentials of 1.6–2.0 V and oxygen-saturated acidic medium with a low pH value of 2–4). Performance degradation of PEMECs originating from corrosion of these metallic BPs can be summarized as follows: (i) Metal cations poisoning: owing to the chemical instability of stainless steels, copper and aluminum in PEMECs, the corresponding metal ions of these metals (e.g., Fe^{3+}, Cu^{2+} and Al^{3+}) are released with anodic corrosion, followed by migration towards the cathode (Figure 6a) [92]. The metal cations occupy ion exchange sites both for the PEM electrolyte and the ionomers of the catalyst layer, thereby decreasing H^+ conductivity and increasing the cell overpotential [93,94]. (ii) Increase in interfacial contact resistance (ICR) for stainless steels: passivation of stainless steels promotes the formation of the poorly conductive Cr_2O_3 film on the surface. Bare SS 316L BPs can be corroded even at a relatively mild condition of 1 V (vs. standard hydrogen electrode (SHE)) [95], as shown in Figure 6b,c. Therefore, these metallic BPs need to have their electrochemical stability substantially improved for use in PEM-based cells. Noble metals such as Pt or Au and transition metals like Nb or Ti, which have excellent corrosion tolerance, are commonly used as coating materials for metallic BPs.

3.2.1. Application of VPS-Sprayed Ti Coatings

Due to the existence of coating defects like pinholes and the occurrence of pitting corrosion, a thin film of Nb as conventionally deposited via magnetron sputtering (MS) is still far from satisfactory for use on BPs of PEMECs [31,33]. This problem can be solved by depositing a thicker metal interlayer via VPS (with pinholes being largely eliminated), which acts as an additional barrier to the corrosive medium. Because of its cost-effectiveness and capability of forming passivating films, titanium is considered a good choice for

this interlayer. A reliable bi-layer coating strategy is therefore often adopted, which can be described as follows: a thin top-layer possessing superior corrosion resistance and excellent electrical conduction and a VPS-coated thick interlayer for inhibiting penetration of corrosive medium.

The German Aerospace Center [34] first investigated the effect of VPS spraying parameters on the microstructure and corrosion resistance of Ti coatings. Increasing plasma enthalpy by adjusting the H_2/Ar ratio (Table 2) was advantageous to enhance the coating density by improving the molten state of Ti powders (grain size of feedstock < 45 μm). Therefore, the highest plasma enthalpy applied (21.27 MJ kg^{-1}) resulted in the densest microstructure and the best corrosion resistance of Ti coating on stainless steels. Figure 6d illustrates the potentiodynamic polarization curves of Ti coatings produced with varied enthalpies [34]. On the basis of optimized VPS-Ti preparation, different bi-layer coatings, such as Au/Ti [32], Pt/Ti [31] and Nb/Ti [33,96], were further developed. Au/Ti coatings deposited by electroplating initially exhibited excellent corrosion resistance, but detachment of the Au top-layer occurred after 6 h corrosion testing at 2 V vs. SHE (Figure 6e) [32]. To enhance the binding between noble metal top-layer and Ti interlayer, electroplating was substituted with magnetron sputtering (MS) to deposit the top layer. As a result, the MS-Pt coated VPS-Ti/SS samples were successfully operated for over 1000 h at 1 A cm^{-2} without spalling of Pt coating (Figure 6f). Moreover, the low ICR of Ti/SS, Pt/SS and Pt/Ti/SS proved that the Pt top layer effectively prevented titanium from oxidation [31]. The manufacturing cost of the coating can be reduced by replacing the noble metal top layer with Nb. The Ti/Nb coating showed a very low corrosion current of 0.40 and 0.25 μA cm^{-2} (Figure 6g,h) before and after potentiostatic polarization tests (6 h, 2 V vs. SHE), respectively [33]. Moreover, being evaluated within a practical electrolysis cell, the Ti/Nb coated SS BPs exhibited good stability during 14,000 h testing (1 A cm^{-2}, 1 bar and 65 °C) with an average decay rate of 5.5 μV h^{-1} obtained (Figure 6i) [39]. In sum, combining the advantages of a VPS-Ti interlayer and a functional top layer, the bi-layered coating is a highly promising strategy for endowing BPs with excellent stability and electrical properties.

3.2.2. Application of VPS-Sprayed Nb Coatings

Taking advantage of the better corrosion resistance of Nb than Ti, a simplified VPS coating process using a one-step coating of an Nb single-layer to replace the two-step Ti/Met bi-layer is proposed by the German Aerospace Center. They used the same spraying parameters as VPS-Ti coating to deposit Nb coating (particle size: 45 μm). According to their study [97], the Nb coating with a thickness of 31 μm (Figure 6j) could provide sufficient protection for metallic BPs (Figure 6k) with a low corrosion current < 0.1 μA cm^{-2} being achieved. Furthermore, a pore-closing or sealing process (i.e., filling the open pores with sealing materials) may be needed to improve the corrosion resistance of the VPS-sprayed Nb coatings, considering the possibility of open pores' existence. The Nb-coated Cu-based BPs were also evaluated by assembling into an electrolysis cell, which demonstrated equal i-V performance to that of a commercial electrolysis cell (Siemens). The polarization curve obtained from the electrolyzer using the VPS-Nb coated Cu BPs is shown in Figure 6l. The VPS-Nb coatings were also prepared on stainless steel-based BPs to investigate their applicability in PEMECs. The electrolysis cell operated with VPS-Nb (~130 μm) coated stainless steel BPs showed a performance of 1.9 V ± 50 mV at 1 A cm^{-2} over the 14,000 h test. The average degradation rate was approx. 5.5 μV h^{-1}, similar to another electrolysis cell equipped with the Ti/Nb coated stainless steel BPs. The results mentioned above demonstrate the feasibility of the VPS-Nb single-layer coatings for the metallic BPs of PEMECs.
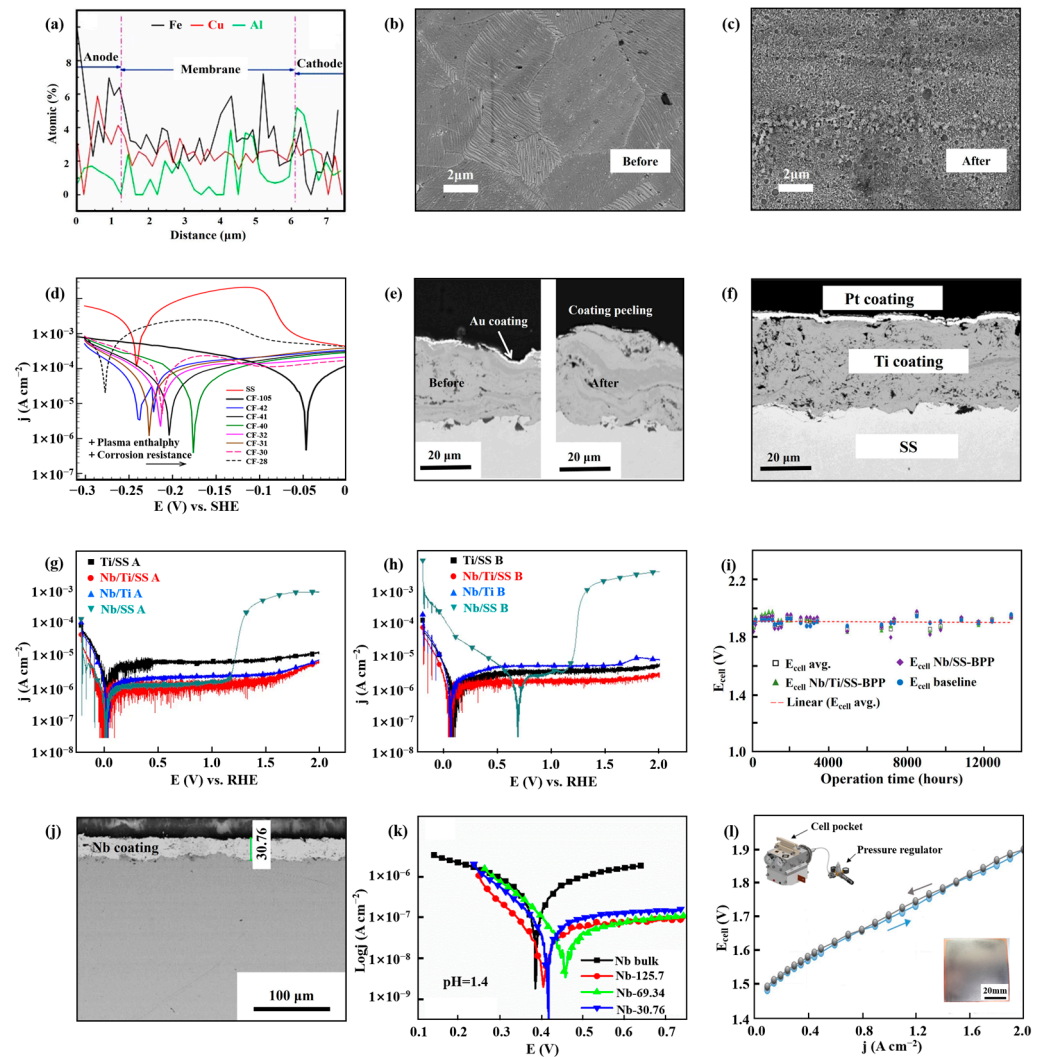
Figure 6. EDX analysis (**a**) [92] of the impurity ion distribution at the cross-section of the contaminated membrane electrode assemblies; surface morphology [95] of bare SS 316L before (**b**) and after aging (**c**) at 1000 mV vs. SHE; potentiodynamic polarization curves (**d**) [34] of Ti coatings produced with different enthalpies; cross-section morphologies of Au-modified Ti/SS sample before and after corrosion test (**e**) [32]; cross-section of Pt-modified Ti/SS (**f**) [31] after 1000 h test at 1 A cm^{-2}, 38 °C; potentiodynamic characteristics of different samples [33] before (**g**) and after (**h**) the chronoamperometric measurements; E_{cell} (**i**) [39] over time of 14,000 h test measured at 1 A cm^{-2}, 1 bar, 65 °C; cross-sectional morphology (**j**) [97] of VPS-Nb coating after test in 0.05 M H$_2$SO$_4$ + 0.1 ppm F$^-$ (pH = 1.4); potentiodynamic polarization curves (**k**) [97] of Nb bulk and Nb coatings after test in 0.05 M H$_2$SO$_4$ + 0.1 ppm F$^-$ (pH = 1.4); polarization curve (**l**) [97] obtained using VPS-Nb coated Cu BPs. Reprinted from [31,32] with permission from IOP Publishing and from [92,95] with permission from Elsevier.

4. High-Velocity Oxygen Fuel Spraying

4.1. Features and Strengths of High-Velocity Oxygen Fuel Spraying

High-velocity oxygen fuel (HVOF) spraying is an advanced coating technology suitable for rapid preparation of dense-structured coatings of metal, alloy and ceramics without oxidizing or decomposing. The detailed processes of HOVF spraying are described as follows [43]: the fuel (such as propane, acetylene, kerosene or propylene) and high-pressure oxygen are evenly mixed and violently burned in the combustion chamber to generate a high-pressure flame, which is then accelerated into a supersonic flame stream (velocity of 400–1000 m s^{-1} or even higher) [45] through the Laval nozzle. The supersonic flame

accelerates and heats the feedstock materials fed into this flame to be of a molten or semi-molten state. These molten or semi-molten particles are then sprayed onto the substrate to be solidified into a coating after cooling. In comparison to APS or VPS, HVOF spraying presents two distinct features: (i) Lower flame temperature: The HVOF flame temperature (<4000 °C) is significantly lower than that of APS/VPS (>10,000 °C). This is beneficial for limiting decomposition of the feedstock materials [9]. (ii) Faster flame velocity: Compared to APS and VPS, HVOF has a much faster flame velocity (Figure 2c), corresponding to a shorter dwell time of in-flight particles. Hence, oxidation of the feedstock materials is effectively inhibited. Further, high flame velocity is conducive to a higher coating density and enhanced corrosion resistance [98]. Therefore, HVOF is appropriate for preparing coatings with feedstock materials sensitive to oxygen or unstable at high temperatures (e.g., metals, alloys or non-oxide ceramics). More importantly, HVOF spraying can offer a significantly higher efficiency of production compared to VPS, which only operates in a vacuum. The above merits make HVOF spraying an attractive technology for the mass production of BP coatings for use in PEM fuel cells and electrolysis cells.

4.2. Application of HVOF-Sprayed Coatings in PEM Cells

The electrochemical corrosion of metallic BPs in PEMFCs occurs mainly on the cathode side (i.e., acidic medium, air or oxygen gas flow and a higher potential than the anode). Meanwhile, for PEMECs, BPs of the anode side have an even harsher operating condition (i.e., acidic medium saturated with pure oxygen and working potentials up to 2.0 V or even higher), making higher demands for resistance to electrochemical oxidation and corrosion. For both PEM-based cells, performance degradation originating from metallic BPs includes [99] an increase in interfacial contact resistance (ICR) due to surface oxidation of BPs, an increase in ohmic resistance in PEM electrolyte and polarization resistance in electrodes due to the poisoning effect of the dissolved metal cations. In order to protect BPs from corrosion, a variety of low melting temperature alloys (e.g., NiCr [100], Co(Ni)CrAlY [100]) and non-oxide ceramics (e.g., NiCrBSi [100], Cr_3C_2 [101]) have been used to coat the metallic BPs by means of the HVOF spraying method.

El-Khatib et al. [102] first employed HVOF to deposit stainless steel coatings (powder size: 20–40 μm) on aluminum substrates, obtaining a low porosity (~1.3%) coating with corrosion resistance similar to that of bulk stainless steels. This work proved the feasibility of HVOF (alternative to vacuum deposition) for preparing dense protective coatings against corrosion, although the inherent property of stainless-steel coating materials is insufficient for use in PEM fuel cells or electrolysis cells. Madadi et al. [100] deposited NiCr, NiCrBSi and CoCrAlY coatings (average grain size of three powders: 25–55 μm) to protect Al BPs and evaluated the performance of these coatings. No metal oxides can be detected in the coating layers, indicating hardly any oxidation occurred during the HVOF spraying process. Correspondingly, all coatings showed good electrical conduction properties (Figure 7a), with the ICR value measured to be 30, 20 and 140 mΩ cm^2 for the NiCr, NiCrBSi and CoCrAlY coating, respectively. All these dense, structured coatings exhibited a low corrosion current (Figure 7b), while the lowest one was obtained on NiCrBSi (4.95×10^{-5} A cm^{-2}). A PEMFC single cell equipped with the NiCrBSi-coated BPs exhibited the highest output power and optimal stability (Figure 7c). Similarly, in another experiment, a PEMFC single cell tested with the HVOF-$Ni_{65}Cr_{15}P_{16}B_4$ coated BPs demonstrated comparable i-V performances to the PEMFC cells using the conventional graphite BPs (Figure 7d) [103]. These studies suggest that HVOF spraying is a very promising technology for coating the BPs of PEM cells.

Similar to other thermal spraying methods, HVOF should be carefully optimized in detailed spraying processes and operation parameters in order to achieve a high-quality protective coating. Generally, overheating of the in-flight particles would promote the decomposition of the feedstock materials, therefore deteriorating the resultant coating performances in terms of defective microstructure and poor electrical conduction. On the other hand, insufficient melting of the in-flight particles can result in decreased coating

porosity and, consequently, poor corrosion resistance. Therefore, it is crucial to precisely control the oxygen/fuel ratio and spraying distance, two factors that determine the flame temperature and velocity of the in-flight particles during the HVOF spraying.
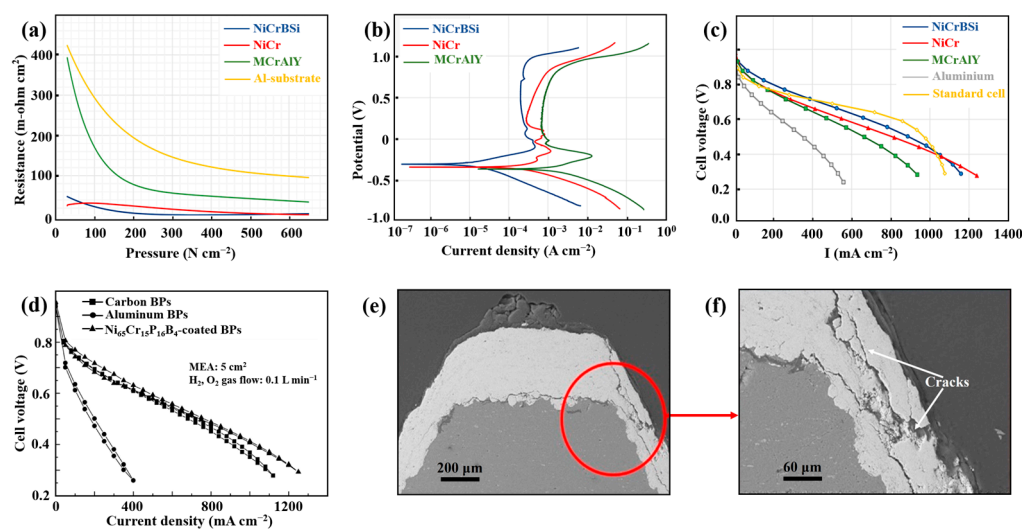
Figure 7. Interfacial contact resistance of the BPs (**a**) [100]; polarization curves (**b**) [100] of the NiCr, NiCrBSi and (Co,Ni)CrAlY coatings; I-V curves (**c**) [100] of the PEMFC single cell tested with graphite, Al, NiCrBSi, NiCr or (Co,Ni)CrAlY coated BPs; I-V curves [103] of the single cell (**d**) tested with carbon, Al and $Ni_{65}Cr_{15}P_{16}B_4$ metallic glass BPs after 50 repetition; cross-sectional morphologies of a rib structure of BPs (**e**); cracks in coating at the rib edge (**f**) [9]. Reprinted from [9] with permission from Elsevier.

However, there are still some problems to be addressed in the preparation of coatings for BPs through the HVOF spraying process, particularly for the ones involving flow fields with deep channels or sharp edge/corner structures. In order to evenly distribute the fuels and oxidants throughout the entire cell area, flow fields are often fabricated in various structural designs on the surface of BPs. The surface of BPs is, therefore, not even, which brings additional difficulty in achieving uniform and defect-free coatings, depending on the specific curvature of the local structure in flow fields. For example, in the preparation of Cr_3C_2 coatings [101] on metallic BPs via HVOF spraying, micro-cracks occurred in the coating at the rib edge of flow fields, impairing the structural integrity of the as-sprayed coating. Cross-sectional morphologies of the coating defects at a rib edge of BPs are shown in Figure 7e,f [9]. These defects will allow the corrosive medium to penetrate the vulnerable aluminum substrate, resulting in corrosion. Therefore, the spraying process and specific parameters (including but not limited to the flame temperature, velocity, feedstock, angle, cycle, etc.) need to be carefully optimized further in order to make HVOF technology appreciable for coating BPs with complicated flow-field structures.

5. Conclusions

By using low-cost and easy-to-process metal materials (such as stainless steel, aluminum or copper) as substrates of BPs for use in hydrogen fuel cells and water electrolysis cells, the manufacturing costs can be significantly reduced, thereby promoting the large-scale application of these green energy technologies. However, these materials would undergo severe corrosion during cell operation, resulting in long-term performance degradation. For SOFCs and SOECs, the formation of a poorly conductive oxide layer, which consists of a Cr_2O_3 inner layer and a $MnCr_2O_4$ outer layer, will increase the BPs' ohmic resistance and decrease the overall cell efficiency. Additionally, the solid Cr_2O_3 could be converted into gaseous Cr-species, which subsequently poison the air electrode by depositing at the air electrode–electrolyte–gas triple-phase boundary (air electrode: $La_{1-x}Sr_xMnO_3$) or other degradation mechanisms for (La-Sr)CoO$_3$, (La-Sr)(Co,Fe)O$_3$, etc.

For PEMFCs/PEMECs, metal ions (e.g., Fe^{3+}, Al^{3+} or Cu^{2+}) originating from corrosion can move towards the anode of fuel cells or cathode of electrolysis cells under the electric field. These metal ions could seize the proton transport sites, thereby reducing the proton conductivity of the electrolyte membrane. Meanwhile, a protective Cr_2O_3 layer formed on the surface of the stainless steel substrates will increase the ohmic resistance of BPs. Therefore, it is crucial to restrict the corrosion of BPs. Applying a protective coating is an effective solution to address this challenge. Thermal spraying methods like APS, VPS and HVOF spraying, etc., are the most commonly used technologies for coating metallic BPs.

APS-sprayed rare earth perovskite or spinel oxide coatings have been widely employed in protecting FSS-based BPs of SOFCs/SOECs from thermal oxidations. The coating composition, microstructure and overall performance rely on spraying process control. Increasing the absorbed heat of powders is advantageous to improve the coating density of both $La_{1-x}Sr_xMnO_3$ and Mn-Co spinel. However, with an increase in the absorbing heat, phase decomposition of $La_{1-x}Sr_xMnO_3$ powder particles will occur, resulting in lower electrical conductivity of the as-sprayed coating. Moreover, the hygroscopic decomposition product (i.e., La_2O_3) can promote absorption/transport of water molecules and thereby raise the reaction rate from solid Cr_2O_3 to gaseous Cr species, deteriorating the high-temperature oxidation resistance of the as-sprayed coating. Similarly, phase decomposition of Mn-Co spinel will occur and decrease the electrical conductivity due to the formation of the low-conductivity (Mn,Co)O rock salt phase. Additionally, a higher absorbed heat normally implies a faster cooling rate and more defects in the coatings. The defects can provide channels for corrosive medium penetration through the as-sprayed coatings, thereby deteriorating the high-temperature oxidation resistance. Therefore, the adoption of appropriate spraying parameters is crucial to obtaining a high-quality coating for the protection of BPs.

VPS is commonly used to deposit metal-based coatings for BPs, particularly for use in PEM cells. A higher plasma enthalpy will be helpful to improve the melting state of the metal powders and enhance the coating density. Meanwhile, pore-closing post-treatment will benefit the further improvement in corrosion resistance of the as-sprayed coatings. The VPS-derived single-layer-Nb and double-layer-Ti/Nb coatings on stainless steel BPs combined with pore-closing treatment have demonstrated good corrosion resistance, electrical conductivity and stability in the practical PEM water electrolysis tests.

HVOF spraying is a cost-effective technology suitable for preparing low-melting temperature metals or non-oxide ceramics/cermet coatings on BPs, particularly for those of PEMFCs or PEMECs. During the spraying, the overheating and insufficient melting of powder particles can deteriorate both the structure and performance of the coatings. The former will lead to powder decomposition, and the latter will increase the coating porosity. Hence, the main influencing factors, such as oxygen/fuel ratio and spraying distance, should be optimized to obtain a desirable protective coating for the BPs.

Conflicts of Interest: The authors declare no conflicts of interest.

References

1. Chen, K.F.; Jiang, S.P. Review-materials degradation of solid oxide electrolysis cells. *J. Electrochem. Soc.* **2016**, *163*, F3070–F3083. [CrossRef]
2. Teuku, H.; Alshami, I.; Goh, J.; Masdar, M.S.; Loh, K.S. Review on bipolar plates for low-temperature polymer electrolyte membrane water electrolyzer. *Int. J. Energy Res.* **2021**, *45*, 20583–20600. [CrossRef]
3. Dihrab, S.S.; Sopian, K.; Alghoul, M.A.; Sulaiman, M.Y. Review of the membrane and bipolar plates materials for conventional and unitized regenerative fuel cells. *Renew. Sust. Energy Rev.* **2009**, *13*, 1663–1668. [CrossRef]
4. Hermann, A.; Chaudhuri, T.; Spagnol, P. Bipolar plates for PEM fuel cells: A review. *Int. J. Hydrogen Energy* **2005**, *30*, 1297–1302. [CrossRef]
5. Weber, A.; Ivers-Tiffée, E. Materials and concepts for solid oxide fuel cells (SOFCs) in stationary and mobile applications. *J. Power Sources* **2004**, *127*, 273–283. [CrossRef]
6. Antunes, R.A.; Oliveira, M.C.L.; Ett, G.; Ett, V. Corrosion of metal bipolar plates for PEM fuel cells: A review. *Int. J. Hydrogen Energy* **2010**, *35*, 3632–3647. [CrossRef]
7. Yue, M.; Lambert, H.; Pahon, E.; Roche, R.; Jemei, S.; Hissel, D. Hydrogen energy systems: A critical review of technologies, applications, trends and challenges. *Renew. Sust. Energy Rev.* **2021**, *146*, 111180. [CrossRef]
8. Ebbesen, S.D.; Jensen, S.H.; Hauch, A.; Mogensen, M.B. High temperature electrolysis in alkaline cells, solid proton conducting cells, and solid oxide cells. *Chem. Rev.* **2014**, *114*, 10697–10734. [CrossRef] [PubMed]
9. Hung, Y.; Tawfik, H.; Mahajan, D. Durability and characterization studies of chromium carbide coated aluminum fuel cell stack. *Int. J. Hydrogen Energy* **2016**, *41*, 12273–12284. [CrossRef]
10. Carmo, M.; Fritz, D.L.; Mergel, J.; Stolten, D. A comprehensive review on PEM water electrolysis. *Int. J. Hydrogen Energy* **2013**, *38*, 4901–4934. [CrossRef]
11. Wang, Y.; Pang, Y.; Xu, H.; Martinez, A.; Chen, K.S. PEM Fuel cell and electrolysis cell technologies and hydrogen infrastructure development—A review. *Energy Environ. Sci.* **2022**, *15*, 2288–2328. [CrossRef]
12. Golkhatmi, S.Z.; Asghar, M.I.; Lund, P.D. A review on solid oxide fuel cell durability: Latest progress, mechanisms, and study tools. *Renew. Sust. Energy Rev.* **2022**, *161*, 112339. [CrossRef]
13. Ardigo, M.R.; Popa, I.; Chevalier, S.; Girardon, P.; Perry, F.; Laucournet, R.; Brevet, A.; Desgranges, C. Effect of coatings on long term behaviour of a commercial stainless steel for solid oxide electrolyser cell interconnect application in H_2/H_2O atmosphere. *Int. J. Hydrogen Energy* **2014**, *39*, 21673–21677. [CrossRef]
14. Mao, J.W.; Wang, E.H.; Wang, H.W.; Ouyang, M.G.; Chen, Y.P.; Hu, H.R.; Lu, L.G.; Ren, D.S.; Liu, Y.D. Progress in metal corrosion mechanism and protective coating technology for interconnect and metal support of solid oxide cells. *Renew. Sust. Energy Rev.* **2023**, *185*, 113597. [CrossRef]
15. Singh, M.; Zappa, D.; Comini, E. Solid oxide fuel cell: Decade of progress, future perspectives and challenges. *Int. J. Hydrogen Energy* **2021**, *46*, 27643–27674. [CrossRef]
16. Sharaf, O.Z.; Orhan, M.F. An overview of fuel cell technology: Fundamentals and applications. *Renew. Sust. Energy Rev.* **2014**, *32*, 810–853. [CrossRef]
17. Feng, Q.; Yuan, X.Z.; Liu, G.Y.; Wei, B.; Zhang, Z.; Li, H.; Wang, H.J. A review of proton exchange membrane water electrolysis on degradation mechanisms and mitigation strategies. *J. Power Sources* **2017**, *366*, 33–55. [CrossRef]
18. Lee, H.; Kim, U.S.; Kim, S.D.; Woo, S.K.; Chung, W.J. SiO_2-B_2O_3-BaO-WO_3 glasses with varying Al_2O_3 content as a sealing material for reversible solid oxide fuel cells. *Ceram. Int.* **2020**, *46*, 18256–18261. [CrossRef]
19. Liu, D.Y.; Geng, S.J.; Chen, G.; Wang, F.H. NiO/$NiFe_2O_4$ dual-layer coating on pre-oxidized SUS 430 steel interconnect. *Int. J. Hydrogen Energy* **2022**, *47*, 21462–21471. [CrossRef]
20. Gago, A.S.; Lettenmeier, P.; Stiber, S.; Ansar, A.S.; Wang, L.; Friedrich, K.A. Cost-effective PEM electrolysis: The quest to achieve superior efficiencies with reduced investment. *ECS Trans.* **2018**, *85*, 3–13. [CrossRef]
21. Otomo, J.; Oishi, J.; Mitsumori, T.; Iwasaki, H.; Yamada, K. Evaluation of cost reduction potential for 1 kW class SOFC stack production: Implications for SOFC technology scenario. *Int. J. Hydrogen Energy* **2013**, *38*, 14337–14347. [CrossRef]
22. Jung, H.Y.; Huang, S.Y.; Ganesan, P.; Popov, B.N. Performance of gold-coated titanium bipolar plates in unitized regenerative fuel cell operation. *J. Power Sources* **2009**, *194*, 972–975. [CrossRef]
23. Carlson, E.J.; Yang, Y.; Fulton, C. *Solid Oxide Fuel Cell Manufacturing Cost Model: Simulating Relationships between Performance, Manufac-Turing and Cost of Production*; Technical Report; OSTI: Oak Ridge, TN, USA, 2004. [CrossRef]
24. Shen, Z.J.; Rong, J.; Yu, X.H. $Mn_xCo_{3-x}O_4$ spinel coatings: Controlled synthesis and high temperature oxidation resistance behavior. *Ceram. Int.* **2020**, *46*, 5821–5827. [CrossRef]
25. Stiber, S.; Sata, N.; Morawietz, T.; Ansar, S.A.; Jahnke, T.; Lee, J.K.; Bazylak, A.; Fallisch, A.; Gago, A.S.; Friedrich, K.A. A high-performance, durable and low-cost proton exchange membrane electrolyser with stainless steel components. *Energy Environ. Sci.* **2022**, *15*, 109–122. [CrossRef]
26. Jiang, S.P.; Chen, X.B. Chromium deposition and poisoning of cathodes of solid oxide fuel cells-A review. *Int. J. Hydrogen Energy* **2014**, *39*, 505–531. [CrossRef]

27. Lædre, S.; Mendizabal, L.; Kongstein, O.E.; Oedegaard, A.; Karoliussen, H.; Seland, F. Ta-ITO Coated titanium bipolar plates for proton exchange membrane water electrolyzers. *J. Electrochem. Soc.* **2022**, *169*, 034504. [CrossRef]

28. Fan, H.Q.; Shi, D.D.; Wang, X.Z.; Luo, J.L.; Zhang, J.Y.; Li, Q. Enhancing through-plane electrical conductivity by introducing Au microdots onto TiN coated metal bipolar plates of PEMFCs. *Int. J. Hydrogen Energy* **2020**, *45*, 29442–29448. [CrossRef]

29. Zhu, J.H.; Chesson, D.A.; Yu, Y.T. Review-$(Mn,Co)_3O_4$-based spinels for SOFC interconnect coating application. *J. Electrochem. Soc.* **2021**, *168*, 114519. [CrossRef]

30. Salehmin, M.N.I.; Husaini, T.; Goh, J.; Sulong, A.B. High-pressure PEM water electrolyser: A review on challenges and mitigation strategies towards green and low-cost hydrogen production. *Energy Convers. Manag.* **2022**, *268*, 115985. [CrossRef]

31. Gago, A.S.; Ansar, S.A.; Saruhan, B.; Schulz, U.; Lettenmeier, P.; Canas, N.A.; Gazdzicki, P.; Morawietz, T.; Hiesgen, R.; Arnold, J.; et al. Protective coatings on stainless steel bipolar plates for proton exchange membrane (PEM) electrolysers. *J. Power Sources* **2016**, *307*, 815–825. [CrossRef]

32. Gago, A.S.; Ansar, A.S.; Gazdzicki, P.; Wagner, N.; Arnold, J.; Friedrich, K.A. Low cost bipolar plates for large scale PEM electrolyzers. *ECS Trans.* **2014**, *64*, 1039–1048. [CrossRef]

33. Lettenmeier, P.; Wang, R.; Abouatallah, R.; Saruhan, B.; Freitag, O.; Gazdzicki, P.; Morawietz, T.; Hiesgen, R.; Gago, A.S.; Friedrich, K.A. Low-cost and durable bipolar plates for proton exchange membrane electrolyzers. *Sci. Rep.* **2017**, *7*, 44035. [CrossRef] [PubMed]

34. Gago, A.S.; Ansar, A.S.; Wagner, N.; Arnold, J.; Friedrich, K.A. Titanium Coatings Deposited by Thermal Spraying for Bipolar Plates of PEM Electrolysers 4th European PEFC and H_2 Forum. Lucerne Switzerland. 2013. Available online: https://elib.dlr.de/92736/1/Chapter-06_EFCF-2013-Session-A07.pdf (accessed on 13 February 2024).

35. Feng, K.; Li, Z.G.; Sun, H.L.; Yu, L.; Cai, X.; Wu, Y.X.; Chu, P.K. C/CrN multilayer coating for polymer electrolyte membrane fuel cell metallic bipolar plates. *J. Power Sources* **2013**, *222*, 351–358. [CrossRef]

36. Zhang, D.M.; Duan, L.T.; Guo, L.; Wang, Z.Y.; Zhao, J.; Tuan, W.H.; Niihara, K. TiN-coated titanium as the bipolar plate for PEMFC by multi-arc ion plating. *Int. J. Hydrogen Energy* **2011**, *36*, 9155–9161. [CrossRef]

37. Yoo, J.; Woo, S.K.; Yu, J.H.; Lee, S.; Park, G.W. $La_{0.8}Sr_{0.2}MnO_3$ and $(Mn_{1.5}Co_{1.5})O_4$ double layer coated by electrophoretic deposition on Crofer22 APU for SOEC interconnect applications. *Int. J. Hydrogen Energy* **2009**, *34*, 1542–1547. [CrossRef]

38. Hui, R.; Wang, Z.W.; Kesler, O.; Rose, L.; Jankovic, J.; Yick, S.; Maric, R.; Ghosh, D. Thermal plasma spraying for SOFCs: Applications, potential advantages, and challenges. *J. Power Sources* **2007**, *170*, 308–323. [CrossRef]

39. Stiber, S.; Hehemann, M.; Carmo, M.; Müller, M.; Ayers, K.E.; Capuano, C.; Danilovic, N.; Morawietz, T.; Biswas, I.; Gazdzicki, P.; et al. Long-term operation of Nb-coated stainless steel bipolar plates for proton exchange membrane water electrolyzers. *Adv. Energy Sustain. Res.* **2022**, *3*, 2200024. [CrossRef]

40. Piccardo, P.; Spotorno, R.; Geipel, C. Investigation of a metallic interconnect extracted from an SOFC stack after 40,000 h of operation. *Energies* **2022**, *15*, 3548. [CrossRef]

41. Hu, Y.Z.; Yao, S.W.; Li, C.X.; Li, C.J.; Zhang, S.L. Influence of pre-reduction on microstructure homogeneity and electrical properties of APS $Mn_{1.5}Co_{1.5}O_4$ coatings for SOFC interconnects. *Int. J. Hydrogen Energy* **2017**, *42*, 27241–27253. [CrossRef]

42. Butt, M.A. Thin-film coating methods: A successful marriage of high-quality and cost-effectiveness-A brief exploration. *Coatings* **2022**, *12*, 1115. [CrossRef]

43. Oksa, M.; Turunen, E.; Suhonen, T.; Varis, T.; Hannula, S.P. Optimization and characterization of high velocity oxy-fuel sprayed coatings: Techniques, materials, and applications. *Coatings* **2011**, *1*, 17–52. [CrossRef]

44. Tejero-Martin, D.; Rad, M.R.; Mcdonald, A.; Hussain, T. Beyond traditional coatings: A review on thermal-sprayed functional and smart coatings. *J. Therm. Spray Technol.* **2019**, *28*, 598–644. [CrossRef]

45. Faisal, N.H.; Prathuru, A.; Ahmed, R.; Cai, Q.; Horri, B.A.; Rajendran, V.; Hossain, M.; Venkatachalapathy, V.; Katiyar, N.K.; Li, J.; et al. Application of thermal spray coatings in electrolysers for hydrogen production advances, challenges, and opportunities. *ChemNanoMat* **2022**, *8*, e202200384. [CrossRef]

46. Han, S.J.; Chen, Y.K.; Sampath, S. Role of process conditions on the microstructure, stoichiometry and functional performance of atmospheric plasma sprayed La(Sr)MnO_3 coatings. *J. Power Sources* **2014**, *259*, 245–254. [CrossRef]

47. Yan, Q.; Gambino, R.J.; Sampath, S.; Lewis, L.H.; Li, L.; Baumberger, E.; Vaidya, A.; Xiong, H. Effects of zinc loss on the magnetic properties of plasma-sprayed MnZn ferrites. *Acta Mater.* **2004**, *52*, 3347–3353. [CrossRef]

48. Sampath, S. Thermal spray applications in electronics and sensors: Past, present, and future. *J. Therm. Spray Technol.* **2010**, *19*, 921–949. [CrossRef]

49. Shaigan, N.; Qu, W.; Ivey, D.G.; Chen, W. A review of recent progress in coatings, surface modifications and alloy developments for solid oxide fuel cell ferritic stainless steel interconnects. *J. Power Sources* **2010**, *195*, 1529–1542. [CrossRef]

50. Molin, S.; Jasinski, P.; Mikkelsen, L.; Zhang, W.; Chen, M.; Hendriksen, P.V. Low temperature processed $MnCo_2O_4$ and $MnCo_{1.8}Fe_{0.2}O_4$ as effective protective coatings for solid oxide fuel cell interconnects at 750 °C. *J. Power Sources* **2016**, *336*, 408–418. [CrossRef]

51. Mohamed, S.M.; Sanad, M.M.S.; Mattar, T.; El-Shahat, M.F.; Rossignol, C.; Dessemond, L.; Zaidat, K.; Obbade, S. The structural, thermal and electrochemical properties of $MnFe_{1-x-y}Cu_xNi_yCoO_4$ spinel protective layers in interconnects of solid oxide fuel cells (SOFCs). *J. Alloys Compd.* **2022**, *923*, 166351. [CrossRef]

52. Ardigo-Besnard, M.R.; Popa, I.; Chevalier, S. Effect of spinel and perovskite coatings on the long term oxidation of a ferritic stainless steel in H_2/H_2O atmosphere. *Corros. Sci.* **2019**, *148*, 251–263. [CrossRef]

53. Bianco, M.; Caliandro, P.; Diethelm, S.; Yang, S.; Dellai, A.; Vanherle, J.; Steinberger-Wilckens, R. In-situ experimental benchmarking of solid oxide fuel cell metal interconnect solutions. *J. Power Sources* **2020**, *461*, 228163. [CrossRef]

54. Somalu, M.R.; Muchtar, A.; Daud, W.R.W.; Brandon, N.P. Screen-printing inks for the fabrication of solid oxide fuel cell films: A review. *Renew. Sust. Energy Rev.* **2017**, *75*, 426–439. [CrossRef]

55. Tikkanen, H.; Suciu, C.; Wærnhus, I.; Hoffmann, A.C. Dip-coating of 8YSZ nanopowder for SOFC applications. *Ceram. Int.* **2011**, *37*, 2869–2877. [CrossRef]

56. Torabi, A.; Etsell, T.H.; Sarkar, P. Dip coating fabrication process for micro-tubular SOFCs. *Solid State Ion.* **2011**, *192*, 372–375. [CrossRef]

57. Jonas, G. Deposition via dip coating technique of dense yttrium stabilized zirconia layers. *Int. J. Appl. Ceram. Technol.* **2013**, *10*, 79–86.

58. Hsueh, T.H.; Tsai, C.H.; Liu, S.E.; Wang, M.C.; Chang, S.M.; Shiue, A.; Chin, K.Y. $LiCoO_2$ battery electrode fabricated by high deposition-rate atmospheric plasma spraying for lithium battery. *J. Electrochem. Soc.* **2022**, *169*, 100506. [CrossRef]

59. Hassan, M.A.; Mamat, O.B.; Mehdi, M. Review: Influence of alloy addition and spinel coatings on Cr-based metallic interconnects of solid oxide fuel cells. *Int. J. Hydrogen Energy* **2020**, *45*, 25191–25209. [CrossRef]

60. Wu, J.W.; Liu, X.B. Recent development of SOFC metallic interconnect. *J. Mater. Sci. Technol.* **2010**, *26*, 293–305. [CrossRef]

61. Mazur, Ł.; Molin, S.; Dąbek, J.; Durczak, K.; Pyzalski, M.; Brylewski, T. Physicochemical properties of $Mn_{1.45}Co_{1.45}Cu_{0.1}O_4$ spinel coating deposited on the Crofer 22 H ferritic steel and exposed to high-temperature oxidation under thermal cycling conditions. *J. Therm. Anal. Calorim.* **2021**, *147*, 5649–5666. [CrossRef]

62. Grünwald, N.; Sohn, Y.J.; Yin, X.n.; Menzler, N.H.; Guillon, O.R.; Vaßen, R. Microstructure and phase evolution of atmospheric plasma sprayed Mn-Co-Fe oxide protection layers for solid oxide fuel cells. *J. Eur. Ceram. Soc.* **2019**, *39*, 449–460. [CrossRef]

63. Rufner, J.; Gannon, P.; White, P.; Deibert, M.; Teintze, S.; Smith, R.; Chen, H. Oxidation behavior of stainless steel 430 and 441 at 800 °C in single (air/air) and dual atmosphere (air/hydrogen) exposures. *Int. J. Hydrogen Energy* **2008**, *33*, 1392–1398. [CrossRef]

64. Yang, Z.; Walker, M.S.; Singh, P.; Stevenson, J.W.; Norby, T. Oxidation behavior of ferritic stainless steels under SOFC interconnect exposure conditions. *J. Electrochem. Soc.* **2004**, *151*, B669–B678. [CrossRef]

65. Park, M.; Shin, J.S.; Lee, S.; Kim, H.J.; An, H.; Ji, H.I.; Kim, H.; Son, J.W.; Lee, J.H.; Kim, B.K.; et al. Thermal degradation mechanism of ferritic alloy (Crofer 22 APU). *Corros. Sci.* **2018**, *134*, 17–22. [CrossRef]

66. Natsuko, S.; Teruhisa, H.; Xiong, Y.P.; Katsuhiko, Y.; Haruo, K.; Brito, M.E.; Yokokawa, H.; Maruyama, T. Structure and transport property of manganese-chromium-iron oxide as a main compound in oxide scales of alloy interconnects for SOFCs. *Solid State Ion.* **2005**, *176*, 681–686.

67. Jiang, S.P.; Zhang, J.P.; Foger, K. Deposition of chromium species at Sr-doped $LaMnO_3$ electrodes in solid oxide fuel cells II. Effect on O_2 reduction reaction. *J. Electrochem. Soc.* **2000**, *147*, 3195–3205. [CrossRef]

68. Fontana, S.; Chevalier, S.; Caboche, G. Metallic interconnects for solid oxide fuel cell: Performance of reactive element oxide coating during 10, 20 and 30 months exposure. *Oxid. Met.* **2012**, *78*, 307–328. [CrossRef]

69. Report on the Status of the Solid Oxide Fuel Cell Program. Available online: http://www.energy.gov/sites/prod/files/2019/09/f66/EXEC-2019-002655_Signed%20Report%201.pdf (accessed on 13 February 2024).

70. Mazur, Ł.; Ignaczak, J.; Bik, M.; Molin, S.; Sitarz, M.; Aleksander, G.; Brylewski, T. Effectiveness of a dual surface modification of metallic interconnects for application in energy conversion devices. *Int. J. Hydrogen Energy* **2022**, *47*, 6295–6311. [CrossRef]

71. Lim, D.P.; Lim, D.S.; Oh, J.S.; Lyo, I.W. Influence of post-treatments on the contact resistance of plasma-sprayed $La_{0.8}Sr_{0.2}MnO_3$ coating on SOFC metallic interconnector. *Surf. Coat. Tech.* **2005**, *200*, 1248–1251. [CrossRef]

72. Baik, K.H. Effects of plasma-sprayed $La_{0.7}Sr_{0.3}MnO_3$ coating on thermally grown oxide scale and electrical conductivity of Fe-Cr interconnect for SOFCs. *J. Electrochem. Soc.* **2013**, *160*, F560–F565. [CrossRef]

73. Wu, W.; Guan, W.; Wang, G.L.; Liu, W.; Zhang, Q.S.; Chen, T.; Wang, W.G. Evaluation of $Ni_{80}Cr_{20}(La_{0.75}Sr_{0.25})_{0.95}MnO_3$ dual layer coating on SUS 430 stainless steel used as metallic interconnect for solid oxide fuel cells. *Int. J. Hydrogen Energy* **2014**, *39*, 996–1004. [CrossRef]

74. Puranen, J.; Lagerbom, J.; Hyvarinen, L.; Kylmalahti, M.; Himanen, O.; Pihlatie, M.; Kiviaho, J.; Vuoristo, P. The structure and properties of plasma sprayed iron oxide doped manganese cobalt oxide spinel coatings for SOFC metallic interconnectors. *J. Therm. Spray Technol.* **2010**, *20*, 154–159. [CrossRef]

75. Han, S.J.; Pala, Z.; Sampath, S. Plasma sprayed manganese-cobalt spinel coatings: Process sensitivity on phase, electrical and protective performance. *J. Power Sources* **2016**, *304*, 234–243. [CrossRef]

76. Hu, Y.Z.; Gao, J.T.; Li, C.X.; Li, C.J. Thermally sprayed MCO/FeCr24 interconnector with improved stability for tubular segmented-in-series SOFCs. *Appl. Surf. Sci.* **2022**, *587*, 152861. [CrossRef]

77. Waluyo, N.S.; Park, S.S.; Song, R.H.; Lee, S.B.; Lim, T.H.; Hong, J.E.; Ryu, K.H.; Im, W.B.; Lee, J.W. Protective coating based on manganese-copper oxide for solid oxide fuel cell interconnects: Plasma spray coating and performance evaluation. *Ceram. Int.* **2018**, *44*, 11576–11581. [CrossRef]

78. Tomas, M.; Asokan, V.; Puranen, J.; Svensson, J.-E.; Froitzheim, J. Efficiencies of cobalt- and copper-based coatings applied by different deposition processes for applications in intermediate-temperature solid oxide fuel cells. *Int. J. Hydrogen Energy* **2022**, *47*, 32628–32640. [CrossRef]

79. Yang, Z.G.; Xia, G.G.; Maupin, G.D.; Stevenson, J.W. Conductive protection layers on oxidation resistant alloys for SOFC interconnect applications. *Surf. Coat. Tech.* **2006**, *201*, 4476–4483. [CrossRef]

80. Hu, Y.Z.; Li, C.X.; Yang, G.J.; Li, C.J. Evolution of microstructure during annealing of $Mn_{1.5}Co_{1.5}O_4$ spinel coatings deposited by atmospheric plasma spray. *Int. J. Hydrogen Energy* **2014**, *39*, 13844–13851. [CrossRef]

81. Tsai, S.Y.; Fung, K.Z.; Ni, C.T.; Ho, H.C. Dependence of electrical properties on thermal reduction of protecting oxides for SOFC interconnect applications. *ECS Trans.* **2015**, *68*, 1641–1647. [CrossRef]

82. Grünwald, N.; Sebold, D.; Sohn, Y.J.; Menzler, N.H.; Vaßen, R. Self-healing atmospheric plasma sprayed $Mn_{1.0}Co_{1.9}Fe_{0.1}O_4$ protective interconnector coatings for solid oxide fuel cells. *J. Power Sources* **2017**, *363*, 185–192. [CrossRef]

83. Grünwald, N.; Lhuissier, P.; Salvo, L.; Villanova, J.; Menzler, N.H.; Guillon, O.; Martin, C.L.; Vaßen, R. In situ investigation of atmospheric plasma-sprayed Mn-Co-Fe-O by synchrotron X-ray nano-tomography. *J. Mater. Sci.* **2020**, *55*, 12725–12736. [CrossRef]

84. Menzler, N.H.; Sebold, D.; Guillon, O. Post-test characterization of a solid oxide fuel cell stack operated for more than 30,000 hours: The cell. *J. Power Sources* **2018**, *374*, 69–76. [CrossRef]

85. Solid Oxide Fuel Cells. Available online: https://www.energy.gov/fecm/solid-oxide-fuel-cells#:~:text=The%20specific%20 goals%20of%20the%20SOFC%20program%20are:,greater%20than%2060%25%20without%20carbon%20capture%20and%20 storage (accessed on 13 February 2024).

86. Alnegren, P.; Froitzheim, J.; Svensson, J. Degradation of ferritic steel interconnects in SOEC environments. *ECS Trans.* **2013**, *27*, 2261–2270. [CrossRef]

87. Wang, R.F.; Sun, Z.H.; Choi, J.P.; Basu, S.N.; Stevenson, J.W.; Tucker, M.C. Ferritic stainless steel interconnects for protonic ceramic electrochemical cell stacks: Oxidation behavior and protective coatings. *Int. J. Hydrogen Energy* **2019**, *44*, 25297–25309. [CrossRef]

88. Lorenzo, M.M.J.; Kolarik, V.; Kuchenreuther-Hummel, V.; Potschke, M.; Schimanke, D. Oxidation of La-Sr-Mn-coated interconnector alloys for steam electrolysis under pressure in pure oxygen and in pure steam. *Oxid. Met.* **2017**, *88*, 279–290. [CrossRef]

89. Cheng, F.P.; Yu, Y.T.; Lu, Y.; Wang, Z.J.; Ling, Y.H.; Jing, C.; Guan, C.Z.; Wang, J.Q. Performance of CoMnO spinel coating onto 441 SS for SOEC interconnect application. *Coatings* **2022**, *12*, 1723. [CrossRef]

90. Xuan, J.L.; Liu, Y.R.; Xu, L.K.; Bai, S.F.; Xin, Y.L.; Wang, L.; Zhang, G.D.; Su, Y.; Xue, L.L.; Li, L. Investigation of acidity on corrosion behavior and surface properties of SS304 in simulated PEMFC cathode environments. *Int. J. Hydrogen Energy* **2022**, *47*, 22938–22951. [CrossRef]

91. Zheng, X.B.; Ji, H.; Huang, J.O.; Ding, C.X. Plasma sprayed Ti and HA coatings: A comparative study between APS and VPS. *Acta Metall. Sin.* **2005**, *18*, 339–344.

92. Li, N.; Araya, S.S.; Cui, X.T.; Kær, S.K. The effects of cationic impurities on the performance of proton exchange membrane water electrolyzer. *J. Power Sources* **2020**, *473*, 228617. [CrossRef]

93. Li, N.; Araya, S.S.; Kær, S.K. The effect of Fe^{3+} contamination in feed water on proton exchange membrane electrolyzer performance. *Int. J. Hydrogen Energy* **2019**, *44*, 12952–12957. [CrossRef]

94. Wang, X.Y.; Zhang, L.S.; Li, G.F.; Zhang, G.; Shao, Z.G.; Yi, B.L. The influence of ferric ion contamination on the solid polymer electrolyte water electrolysis performance. *Electrochim. Acta* **2015**, *158*, 253–257. [CrossRef]

95. André, J.; Antoni, L.; Petit, J.P.; De, V.E.; Montani, A. Electrical contact resistance between stainless steel bipolar plate and carbon felt in PEFC: A comprehensive study. *Int. J. Hydrogen Energy* **2009**, *34*, 3125–3133. [CrossRef]

96. Lettenmeier, P.; Wang, R.; Abouatallah, R.; Burggraf, F.; Gago, A.S.; Friedricha, K.A. Coated stainless steel bipolar plates for proton exchange membrane electrolyzers. *J. Electrochem. Soc.* **2016**, *163*, F3119–F3124. [CrossRef]

97. Kellenberger, A.; Vaszilcsin, N.; Duca, D.; Dan, M.L.; Duteanu, N.; Morawietz, T.; Biswas, I.; Ansar, S.A.; Gazdzicki, P.; Wirkert, F.J.; et al. Towards replacing titanium with copper in the bipolar plates for proton exchange membrane water electrolysis. *Materials* **2022**, *15*, 1628. [CrossRef] [PubMed]

98. Kawakita, J.; Kuroda, S.; Fukushima, T.; Katanoda, H.; Matsuo, K.; Fukanuma, H. Dense titanium coatings by modified HVOF spraying. *Surf. Coat. Tech.* **2006**, *201*, 1250–1255. [CrossRef]

99. Liu, R.X.; Jia, Q.; Zhang, B.; Lai, Z.G.; Chen, L. Protective coatings for metal bipolar plates of fuel cells: A review. *Int. J. Hydrogen Energy* **2022**, *47*, 22915–22937. [CrossRef]

100. Madadi, F.; Rezaeian, A.; Edris, H.; Zhiani, M. Improving performance in PEMFC by applying different coatings to metallic bipolar plates. *Mater. Chem. Phys.* **2019**, *238*, 121911. [CrossRef]

101. Rendón-Belmonte, M.; Pérez-Quiroz, J.T.; Terán-Guillén, J.; Porcayo-Calderón, J.; Torres-Acosta, A.; Orozco-Gamboa, G. Evaluation of a $Cr_3C_2(NiCr)$ coating deposited on s4400 by means of an HVOF process and used for flow plates of PEM fuel. *Int. J. Electrochem. Sci.* **2012**, *7*, 1079–1092. [CrossRef]

102. El-Khatib, K.M.; Helal, M.O.A.; El-Moneim, A.A.; Tawfik, H. Corrosion stability of SUS316L HVOF sprayed coatings as lightweight bipolar plate materials in PEM fuel cells. *Anti-Corros. Methods Mater.* **2004**, *51*, 136–142. [CrossRef]

103. Kim, S.C.; Yamaura, S.I.; Shimizu, Y.; Nakashima, K.; Igarashi, T.; Makino, A.; Inoue, A. Production of $Ni_{65}Cr_{15}P_{16}B_4$ metallic glass-coated bipolar plate for fuel cell by high velocity oxy-fuel (HVOF) spray coating method. *Mater. Trans.* **2010**, *51*, 1609–1613. [CrossRef]